Author/s:
Gu, J;Yang, S;Liu, JZ;Zhang, L

Title:
Unravelling the atomistic mechanisms underpinning the morphological evolution of Al-alloyed hematite

Date:
2024-02-05

Citation:
Gu, J., Yang, S., Liu, J. Z. & Zhang, L. (2024). Unravelling the atomistic mechanisms underpinning the morphological evolution of Al-alloyed hematite. Nanoscale, 16 (12), pp.5976-5987. https://doi.org/10.1039/d3nr05765h.

Persistent Link:
https://hdl.handle.net/11343/350290

Volume 16
Number 12
28 March 2024
Pages 5857-6316

Nanoscale

rsc.li/nanoscale

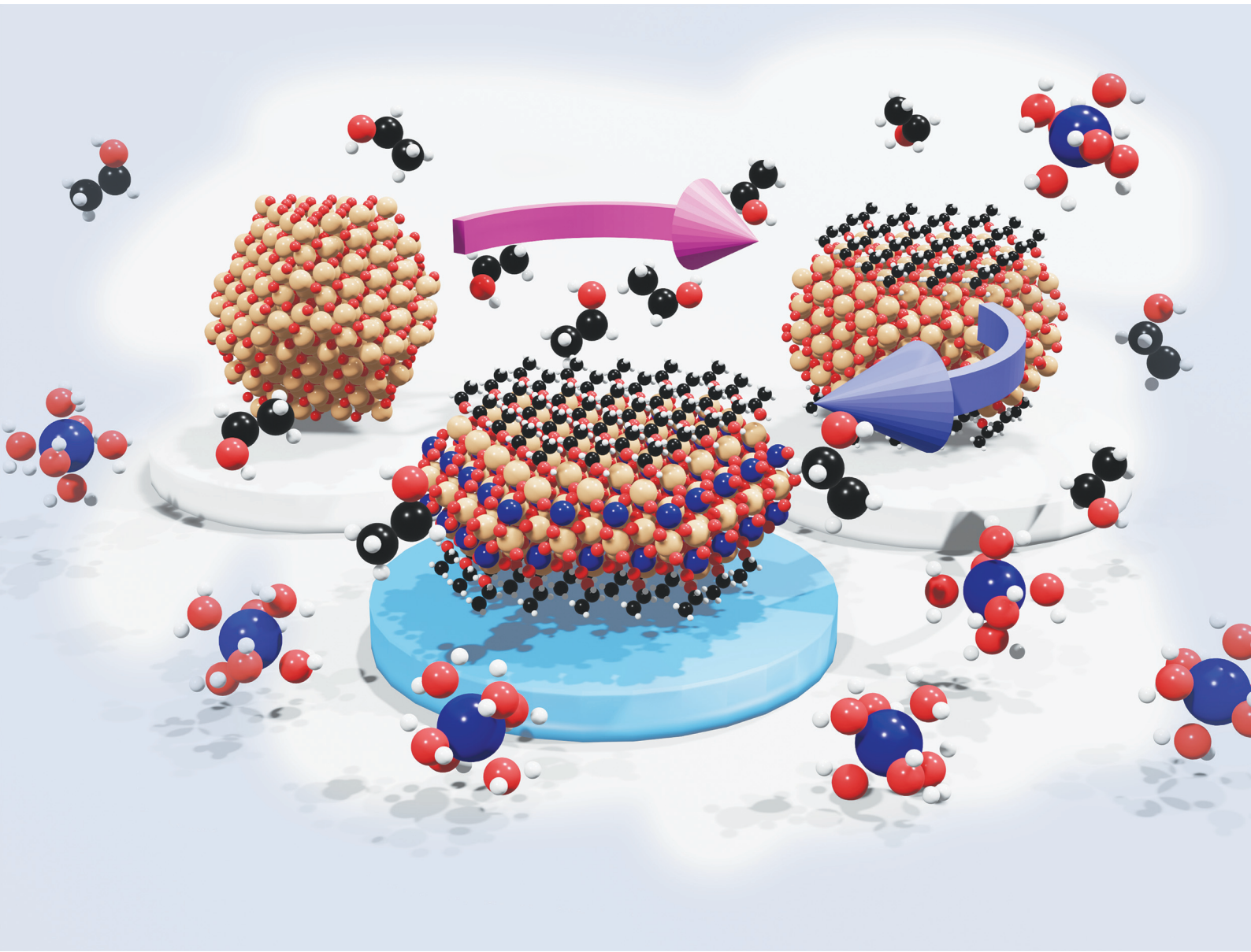

ISSN 2040-3372

ROYAL SOCIETY OF CHEMISTRY

PAPER
Jefferson Zhe Liu, Lian Zhang *et al.*
Unravelling the atomistic mechanisms underpinning the morphological evolution of Al-alloyed hematite

NCNST

Nanoscale

ROYAL SOCIETY OF CHEMISTRY

PAPER

View Article Online
View Journal | View Issue

Cite this: *Nanoscale*, 2024, **16**, 5976

Unravelling the atomistic mechanisms underpinning the morphological evolution of Al-alloyed hematite†

Jinxing Gu,[a] Sasha Yang,[a] Jefferson Zhe Liu *[b] and Lian Zhang *[a]

Received 13th November 2023,
Accepted 4th February 2024

DOI: 10.1039/d3nr05765h

rsc.li/nanoscale

Hydrothermal synthesis based upon the use of Al^{3+} as the dopant and/or ethanol as the solvent is effective in promoting the growth of hematite into nanoplates rich in the (001) surface, which is highly active for a broad range of catalytic applications. However, the underpinning mechanism for the flattening of hematite crystals is still poorly comprehended. To close this knowledge gap, in this work, we have attempted intensive computational modelling to construct a binary phase diagram for Fe_2O_3–Al_2O_3 under typical hydrothermal conditions, as well as to quantify the surface energy of hematite crystal upon coverage with Al^{3+} and ethanol molecules. An innovative coupling of density functional theory calculation, cluster expansion and Monte Carlo simulations in analogy to machine learning and prediction was attempted. Upon successful validation by experimental observation, our simulation results suggest an optimum atomic dispersion of Al^{3+} within hematite in cases when its concentration is below 4 at% otherwise phase separation occurs, and discrete Al_2O_3 nano-clusters can be preferentially formed. Computations also revealed that the adsorption of ethanol molecules alone can reduce the specific surface energy of the hematite (001) surface from 1.33 to 0.31 J m^{-2}. The segregation of Al^{3+} on the (001) surface can further reduce the specific surface energy to 0.18 J m^{-2}. Consequently, the (001) surface growth is inhibited, and it becomes dominant after the disappearance of other surfaces upon their continual growth. This work provides atomistic insights into the synergistic effect between the aluminium textural promoter and the ethanol capping agent in determining the morphology of hematite nanoparticles. The established computation approach also applies to other oxide-based catalysts in controlling their surface growth and morphology, which are critical for their catalytic applications.

Introduction

Naturally occurring hematite is the most stable form of the oxides of iron,[1] and is also a heterogeneous catalyst for various reactions, including photochemical water-splitting,[2–5] peroxide activation,[6] carbon monoxide oxidation,[7] and water–gas shift reactions.[8–10] Hematite exhibits a surface-dependent catalytic activity, with the (001) surface being the most desirable for the adsorption and photocatalytic degradation of organic pollutants. The (001) surface also favours the electrochemical oxygen evolution reaction due to the feasible formation of oxo intermediates.[11–15] More specifically, the nanoplate-like hematite with high exposure of its (001) surface exhibits superior reaction rates and cycling capabilities as the anode for Li-ion batteries.[16] Density functional theory calculations also revealed the potential uses of the (001) surface for CO_2 reduction, NO reduction, and oxygen reduction reactions.[17–19] Moreover, the (001) surface enables high stability for hematite when it is exposed to N_2, air, humid air, and deionized water.[20]

Doping aluminium with a concentration of less than 15 at% is a proven method in promoting the formation of the (001) surface-dominating hematite nanoparticles.[21,22] The most commonly used method is the co-precipitation of cationic Fe^{3+} and Al^{3+} in an alkaline solution, followed by hydrothermal treatment of the precipitate in a capping agent.[23] With the addition of 5.35 at% Al^{3+},[23] the resulting nanoparticles change to (001) surface-dominating nanoplates. In a similar study with the addition of 9.4 at% Al^{3+}, the proportion of the (001) surface increased from ~44.0% in pure hematite to ~84.8%.[21] Upon the use of 14 at% Al^{3+} and a hydrothermal temperature of 180 °C, Qian *et al.* discovered phase separation as the α-Al_2O_3 nanoparticle emerges.[22] Furthermore, the Fe

[a]*Department of Chemical and Biological Engineering, Monash University, Victoria3800, Australia. E-mail: lian.zhang@monash.edu*
[b]*Department of Mechanical Engineering, Faculty of Engineering and Information Technology, The University of Melbourne, Victoria3010, Australia. E-mail: zhe.liu@unimelb.edu.au*

† Electronic supplementary information (ESI) available. See DOI: https://doi.org/10.1039/d3nr05765h

K-edge extended X-ray absorption fine structure spectroscopy analysis confirmed an increase in the Fe–Fe bond length along the [001] crystal direction by ~4.0% when the Al^{3+} concentration is 9.23 at%.[23] This was claimed to decrease the reticular density along the [001] crystal direction as well as the growth of nanoparticles along this direction, with little being given to articulate the underpinning mechanism. Likewise, Wang *et al.* synthesised pure hematite nanoplates, nanorods, and nanocubes using hydrothermal methods and examined their adsorption density for cationic Al^{3+}, confirming a descending trend of (110) > (012) > (001).[24] Accordingly, the authors proposed that the strong Al^{3+} adsorption density on the (110) and (012) surfaces led to their rapid growth and final disappearance.[24] Additionally, capping agents such as ethanol can effectively promote forming (001) surface-dominating hematite nanoplates.[16,25,26] Chen *et al.* dissolved 1 mmol $FeCl_3{\cdot}6H_2O$ and 0.8 g of sodium acetate into a solution of 10 mL of ethanol and 0.7 mL of water.[25] After hydrothermal treatment at 180 °C for 4 h, round hematite nanoplates with a dominating (001) surface and composed of small nanoparticles in crystallographic orientation were formed. With the hydrothermal duration increased to 7 h, the round hematite nanoplates were converted into perfect hexagonal nanoplates, exhibiting (001) basal surfaces with a width of ~200 nm and a height of ~10 nm. Zong *et al.* further examined the effect of the role of ethanol/water volume ratio on the formation of the (001) surface, noting that the nanoplate shape was only formed when the ethanol/water volume ratio ≥90 : 10.[27] The same authors attributed this phenomenon to the nucleophilic affinity of ethanol to iron atoms on the (001) surface of hematite, which retarded the crystal growth along the [001] direction.[25] However, this conclusion is seemingly distinct from that for the claimed role of Al^{3+}, which was more strongly adsorbed on the other surfaces.[24]

Despite these understandings, the underlying mechanism for the promoting effects of Al^{3+} and capping agent and their combined role in determining the hematite (001) surface domination is still far from complete and even contradictory to one another. In particular, there is a lack of understanding on the atomistic level. According to the Gibbs–Curie–Wulff theorem, the dominance of the (001) surface could be attributed to its least surface energy among those of all other surfaces.[28] Furthermore, due to the difference in ionic radii, substituting Al^{3+} into hematite would cause surface segregation.[29] Surface segregation has been confirmed to decrease the surface energy of $CaTiO_3$ perovskite.[30] Additionally, capping agents could also reduce the surface energy of a preferred surface.[31] In this regard, the phase separation, surface segregation, as well as alteration of surface energy, could be the determining factor for the growth of hematite during hydrothermal synthesis. However, as far as the authors are aware, no study has yet been completed to validate this hypothesis.

In this work, we purposely synthesised five hematite samples under well-controlled hydrothermal conditions where both ethanol and Al^{3+} are present. Differing from the optimum 90% ethanol found elsewhere,[27] the ethanol/water volume ratio was fixed at 30 : 70, and the concentration of Al^{3+} was varied from nil to ~17 at%, covering a full span of the morphological evolution of hematite from standard rhombohedron to round nanoplate. A 24-hour incubation duration was employed to ensure uniform mixing of the two cationic metals and the completion of their growth. In addition, intensive modelling with the combination of density functional theory (DFT) calculations, cluster expansion (CE), and Monte Carlo (MC) simulations was attempted. The active machine learning-like CE model learns from DFT calculations and serves as the energy functional for the MC simulations. The simulation will construct the binary phase diagram of Fe_2O_3–Al_2O_3 in the typical hydrothermal temperature window. This phase diagram complements the traditional experimentally determined phase diagram for Fe_2O_3–Al_2O_3 at high temperatures (*i.e.*, over 643.15 K).[32–34] In addition, the simulation is expected to unveil the spatial distribution of Al^{3+} within the bulk hematite throughout a hundred thousand atoms to construct the hematite surface models. Consequently, by calculating the surface energy of these surface models under the impacts of ethanol adsorption and Al^{3+} surface segregation, the nanoparticle morphology based on the Wulff construction method was constructed and cross-checked with the experimental results. This study specifically aims to reveal the synergy between the textural promoter and the capping agent on the atomistic structure of Al-alloyed hematite. It is also expected to provide a validated computing approach with a machine-learning function to fast-track the prediction and optimisation of the structure of any metal oxide-based catalysts, which is ultimately crucial in establishing a rigorous structure–activity relationship for catalyst design.

Experiments and methods

Synthesis of Al-alloyed hematite

Aluminium-alloyed hematite, abbreviated as $(Fe, Al)_2O_3$ hereafter, was synthesised using the classic co-precipitation and hydrothermal methods. Five samples, namely, FeAl-0, FeAl-1, FeAl-2, FeAl-3, and FeAl-4, were synthesised for Al alloying concentrations of nil, 1.01 at%, 2.88 at%, 6.35 at%, and 17.24 at%, which were calculated as molar percentages of Al. For the capping agent, a mixed ethanol/water solution at a volume ratio of 30 : 70 was used, which is different from the ≥90 : 10 with the co-existence of an additional sodium acetate capping agent.[27] Taking FeAl-1 as an example, 0.24 g of high-purity $Al(NO_3)_3{\cdot}9H_2O$ and 25.14 g of $Fe(NO_3)_3{\cdot}9H_2O$ were dissolved in 100 mL of Milli-Q water, the pH of which was then increased to 6 by adding NaOH (2 mol L^{-1}) dropwise. The slurry was centrifuged and washed three times to obtain the precipitate. Afterwards, along with 45 mL of Milli-Q water and 20 mL of ethanol, the residue was transferred into a Teflon autoclave and incubated at 180 °C for 24 h. Finally, the precipitate was collected, washed, and dried in air at 80 °C for 8 h. All the chemicals used are of reagent-grade and purchased from Sigma-Aldrich. The compositions of the obtained samples

were further determined using an X-ray fluorescence spectrometer (SPECTRO iQ II XRF analyser). XRD (X-ray powder diffraction) patterns were obtained with a Rigaku Miniflex600 instrument using Cu Kα radiation (λ = 1.542 Å) operated at 45 kV and 20 mA from 20° to 70° with a step size of 0.02°. BET (Brunauer–Emmett–Teller) surface areas were measured by N_2 adsorption–desorption at 77 K using a Micromeritics 3Flex instrument. Before measurements, the samples were degassed under vacuum at 300 °C for 4 h. The morphologies of these samples were observed by transmission electron microscopy (TEM) (FEI Tecnai G2 T20), with the generated electron diffraction data being analysed with the assistance of CrysTBox.[35,36] X-ray photoelectron spectra (XPS) were recorded using an AXIS Ultra spectrometer (Escalab 250Xi, Thermo Fisher Scientific, USA) with an Al Kα X-ray source (1486.6 eV). The resultant spectra were calibrated at C 1s of 284.8 eV.

Computational methods

Fig. 1 illustrates the combined computational approach to explore the atomistic knowledge underpinning the evolution of the morphology of hematite with the addition of ethanol and Al^{3+} in the hydrothermal process. The first step involves attempting to obtain the phase diagram of the (Fe, Al)$_2O_3$ alloy system for the temperature-dependent distribution of Al^{3+} within the hematite bulk. Here, the CE and MC simulations were added to overcome DFT's limitations on studying the (Fe, Al)$_2O_3$ alloy with 48 000 Fe/Al atoms at finite temperatures.

For the training of the CE model, an initial database containing ten structures of Al-alloyed bulk hematite and the corresponding mixing energies of these structures was constructed based on the DFT. Subsequently, the CE model was trained to generate the most stable structure at each concentration, which was then subsequently put back into the DFT for validation. For the non-validated structure, it was then added to the database and fed back again into the CE for its training. This iteration repeats until the CE model converges with a cross-validation score of no more than 5 meV per atom.[37] For the simulation here, a total of 125 alloy configurations were finally generated, reaching a low cross-validation score of 3.503 meV per atom for the CE model. Afterwards, the fully trained and converged CE model was used to fast-track the computation of the mixing energy of the (Fe, Al)$_2O_3$ bulk system with 48 000 Fe/Al atoms. Finally, the (Fe, Al)$_2O_3$ canonical ensemble was sampled using the Metropolis Monte Carlo method *via* the CLEASE package to predict the phase diagram at low temperatures.[38] Details can be found in the ESI.†

Second, based on the phase diagram and the distribution of Al^{3+} at the hydrothermal temperature, the surface models, including that of the pure hematite surface, plus those of Al-alloyed, ethanol-adsorbed, and Al-alloyed with ethanol-adsorbed hematite surfaces, were constructed to calculate the specific surface energies using the DFT. Subsequently, the Wulff construction method was attempted to predict the nanoparticle morphology based on the specific surface energies.

For the pure hematite surface, its specific surface energy (γ) is calculated by the following eqn (1):[39]

$$\gamma = \frac{E_{surf} - NE_{bulk}}{2A} + \frac{E'_{surf} - E_{surf}}{A} \quad (1)$$

where E_{bulk} is the energy of bulk hematite per molecular formula unit, E_{surf} is the energy of the slab model without relaxation, E'_{surf} is the energy of the slab model with only the top surface being relaxed, N is the number of molecular formulas the slab model contains, and A is the slab surface area.[39] The alloying of Al^{3+} is expected to stabilise the surface through surface segregation. Thus, the specific surface energy after Al^{3+} alloying was termed γ' and computed as,[30,40]

$$\gamma' = \gamma + \frac{nE_{seg}}{A} \quad (2)$$

where γ is the specific surface energy for the pure hematite surface, E_{seg} is the segregation energy per atom, and n is the number of Al^{3+} ions on the surface. In this work, the E_{seg} is defined as the most negative energy difference between Al^{3+} at the i^{th} site and the eighth site, as per eqn (3). The eighth site, which was chosen for the DFT calculation, has been confirmed a convergence of various sites for the energy difference of Al^{3+} on this site. Accordingly, we assume that the eighth site has reached deep inside the bulk of hematite.

$$E_{seg} = \frac{\min(E_{nAl@i} - E_{nAl@8})}{n} \quad (3)$$

$E_{nAl@i}$ refers to the total energy of the surface when n Al^{3+} occupies the i^{th} site on the surface.

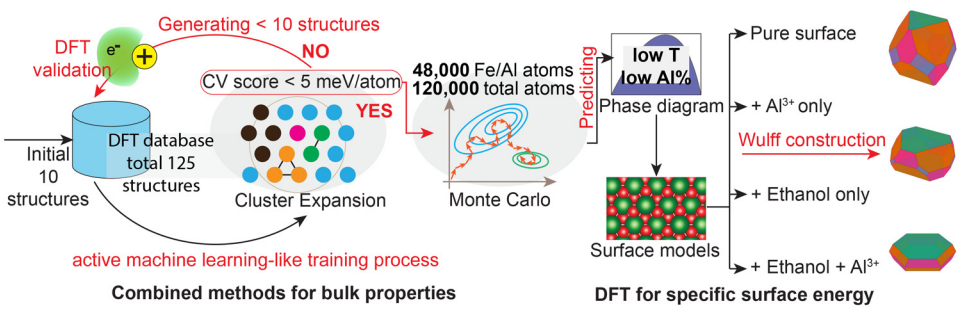

Fig. 1 A combined computational approach including the density functional theory, cluster expansion and Monte Carlo methods for the training and prediction to explore the atomistic mechanisms underpinning the morphological evolution of the (Fe, Al)$_2O_3$ system.

Regarding the adsorption of ethanol on the surface, the specific surface energy of pure hematite after the ethanol adsorption (γ_{eth}) was calculated as:[41–43]

$$\gamma_{eth} = \gamma + \frac{mE_{ads}}{A} \quad (4)$$

where E_{ads} is the adsorption energy per ethanol molecule, and m is the number of ethanol molecules adsorbed. The E_{ads} is defined as:

$$E_{ads} = \frac{E_{m_{eth}} - E_* - mE_{eth}}{m} \quad (5)$$

where E_* is the energy of the surface model, E_{eth} is the total energy of one ethanol molecule, and E_{meth} is the energy of the surface with m ethanol molecules adsorbed. The combined effect of Al and ethanol was simulated by considering the Al segregation on the ethanol-adsorbed surface. The specific surface energy under this combined effect is termed γ'_{eth} and computed as follows:

$$\gamma'_{eth} = \gamma + \frac{mE_{ads}}{A} + \frac{nE'_{seg}}{A} \quad (6)$$

where E'_{seg} is the segregation energy per Al atom when ethanol is also on the surface.

Spin-unrestricted DFT calculations were conducted using the Vienna *ab initio* simulation package (VASP).[44] The exchange–correlation interactions were described using the Perdew–Burke–Ernzerhof functional.[45] To deal with the strong correlation between d electrons of iron, an effective U value of 4.3 eV was adopted.[46–50] The projector-augmented-wave method describes the interactions between electrons and ions. The plane wave basis set with an energy cut-off of 500 eV was adopted. The VASPKIT package was used to generate a k-mesh grid.[51] A k-mesh of 6 × 6 × 3 was used for the hematite unit cell. Similar mesh density was employed for other ordered alloy structures/configurations.[52]

Results and discussion

XRD and TEM bulk analysis of as-synthesised (Fe, Al)$_2$O$_3$

Table 1 shows the physical properties of the five synthesised samples. The XRD patterns in Fig. 2a confirmed that these samples are well-crystallised hematite. More specifically, unlike the findings elsewhere,[23,53] the (110) peak decreased when the Al^{3+} concentration increased. Nevertheless, as shown in Fig. 2b–f, there is an evident morphology evolution upon the increase of Al%. A rhombohedron morphology was observed for most of the nanoparticles formed for the first three samples from pure hematite (FeAl-0) to FeAl-1 with 0.64 at% Al^{3+} and FeAl-2 with 1.84 at% Al^{3+}. These particles are also mostly in single-crystal shape (Fig. S1†). Nevertheless, with a relatively high Al^{3+} concentration ≥6.35 at%, the nanoparticles synthesised are mainly in large and round nanoplate shapes. A similar morphological change was observed elsewhere when the Al^{3+} concentration threshold was around 4.35 at%.[23] Accordingly, the average size of these five samples is increased stably, from 67.27 nm for pure hematite to 77.42 nm for FeAl-2 and 291.71 nm for FeAl-4. In parallel, the aspect ratio of FeAl-3 and FeAl-4 nanoparticles reaches 2.11 and 2.26, echoing their flattened morphology. This finding broadly agrees with one previous study,[27] despite the ethanol/water ratio we used being much lower than theirs.

The high-resolution TEM (HRTEM) images in Fig. 3 reveal the fine details of the roundest nanoplate, FeAl-4 with 17.24 at% Al^{3+}. Fig. 3a and Fig. S2† show the top and side views of the round nanoplates within this sample. For the cyan box region in Fig. 3a, its amplified observation in Fig. 3b confirmed that these round nanoplates are clusters of smaller individual particles with a diameter of 7–8 nm. Such a size is much smaller than the single crystals observed in the first three samples from FeAl-0 to FeAl-1 and FeAl-2. In addition, for the green box region in Fig. 3a, its amplified image in Fig. 3c confirmed that it possesses a multi-layered structure consisting of smaller individual particles with a height of ~5 nm in each layer. Furthermore, on the amplified top view in Fig. 3b, the exposed surfaces of these smaller particles exhibit three lattice fringes for the (110) plane, whilst the side view in Fig. 3c also confirmed that the lattice fringes of these smaller particles belong to the (110) plane. These lattice fringes continue across the smaller particle boundaries, indicating that these small particles are well aligned. More specifically, for the red box region in Fig. 3b, its Fourier transform (FFT) image in Fig. 3d shows the hexagonal symmetry, and its inverse FFT image suggests a honeycomb arrangement for the atoms, which is a typical atom arrangement on the hematite (001) surface.[54,55] The selected area electron diffraction (SAED) analysis of a typical nanoplate, shown in Fig. 3e, confirmed a single-crystal diffraction pattern with its d-spacings along the A, C, and D vectors of around 0.25 nm. This feature aligns well with the {110} plane of pure hematite, whilst the d-spacing

Table 1 Composition, specific surface area (SSA), and aspect ratio of the synthesised samples

Samples	Al at% (XRF)	Al at% (XPS)	Average size (nm)	Aspect ratio	SSA[a] ($m^2\ g^{-1}$)	Calculated SSA[b] ($m^2\ g^{-1}$)
FeAl-0	0.00	0.00	67.27	—	17.71 ± 3.02	19.62
FeAl-1	1.01	7.28	67.68	—	16.64 ± 0.47	19.50
FeAl-2	2.88	7.45	77.42	—	16.61 ± 0.65	17.05
FeAl-3	6.35	13.08	185.39	2.11	8.65 ± 1.40	7.33
FeAl-4	17.24	24.34	291.71	2.26	11.82 ± 1.77	9.90

[a] BET curves are given in Fig. S4.† [b] Detailed calculations can be found in the ESI.†

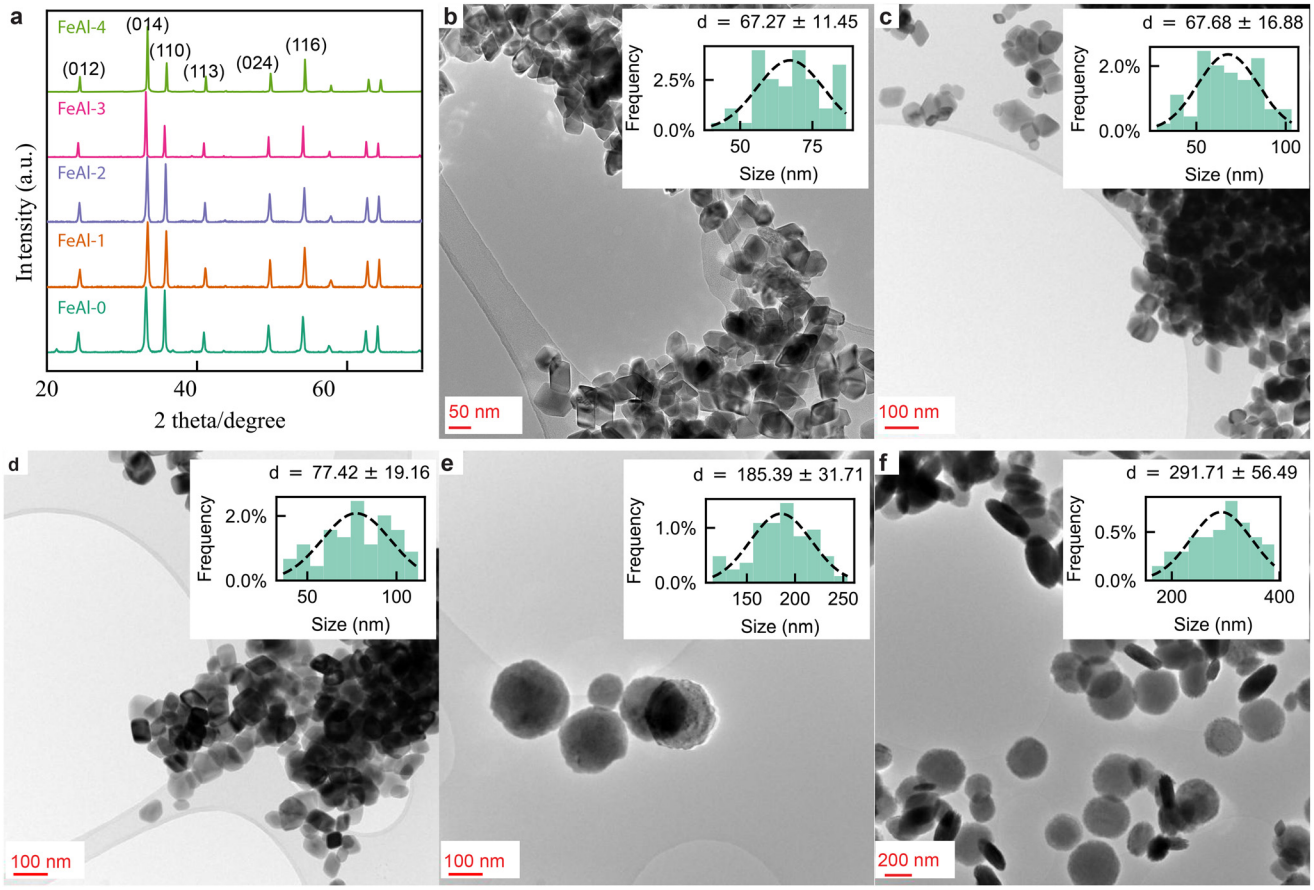

Fig. 2 Structural characterisation of Al-alloyed hematite. (a) XRD patterns of FeAl-0, FeAl-1 (1.01 at%), FeAl-2 (2.88 at%), FeAl-3 (6.35 at%), and FeAl-4 (17.24 at%) samples. (b–f) TEM images of FeAl-0, FeAl-1, FeAl-2, FeAl-3, and FeAl-4, respectively. Inset figures indicate the size distribution measured by TEM.

talong the B vector reaches around 0.14 nm, corresponding to the (030) plane. The zone axis of the SAED pattern was determined to be along the [001] direction of hematite. With all these confirmed observations, it is shown conclusively that all these smaller individual particles are well aligned to form a round monocrystalline shape, with its basal surfaces being the (001) hematite surface.

Regarding the presence of Al, the SAED pattern in Fig. 3f confirmed a discrete corundum (α-Al_2O_3) phase within the FeAl-4 sample. This phase was determined per the ring radii and the corresponding *d*-spacing value, as detailed in Fig. S3† and its two associated tables (Tables S1 and S2†). The discrete corundum phase was also confirmed in FeAl-3, whereas it is indiscernible in other low-Al content samples (Fig. S3†). Under the hydrothermal temperature of 180 °C used here, it is inferred that phase separation occurs in the $(Fe, Al)_2O_3$ system where the atomic concentration of Al^{3+} is no less than 6.35%.

Finally, it is also worth noting that, although Al is widely considered a textural promoter that can increase the specific surface area (SSA) of hematite at the Al% ranging from 0 to 33.33 at%,[56] the data in Table 1 failed to confirm this trend. Instead, the SSA was found to decrease. In particular, the SSA is much smaller for the last two nanoplate-rich samples. Nevertheless, this decreasing trend was also reported by Jiang *et al.* for hematite with less than 7 at% Al^{3+},[57] and by Han *et al.* for 9–15 at% Al^{3+}.[58] This trend also broadly agrees with our simple estimation based on the assumption of cubic crystal structures for the first three samples and cylindrical crystal for the last two, as detailed in Fig. S5.† This variation of SSA and crystal size for hematite is crucial in affecting a variety of applications that are highly size-dependent. For example, hematite nanoparticles of small size show enhanced adsorption of chromium(VI), higher discharge capacity, superior cycling reversibility for lithium-ion batteries, and catalytic performance.[59–61] This will be further explored by us for some specific applications in the future.

XPS surface analysis

The Al 2p XPS profile in Fig. 4a supports the successful alloying of Al into hematite. Referring back to Table 1, for all the five samples, the Al concentration determined *via* XPS surface scanning (spectra in Fig. S6†) is above the corresponding value determined by bulk XRF analysis, supporting the preferred

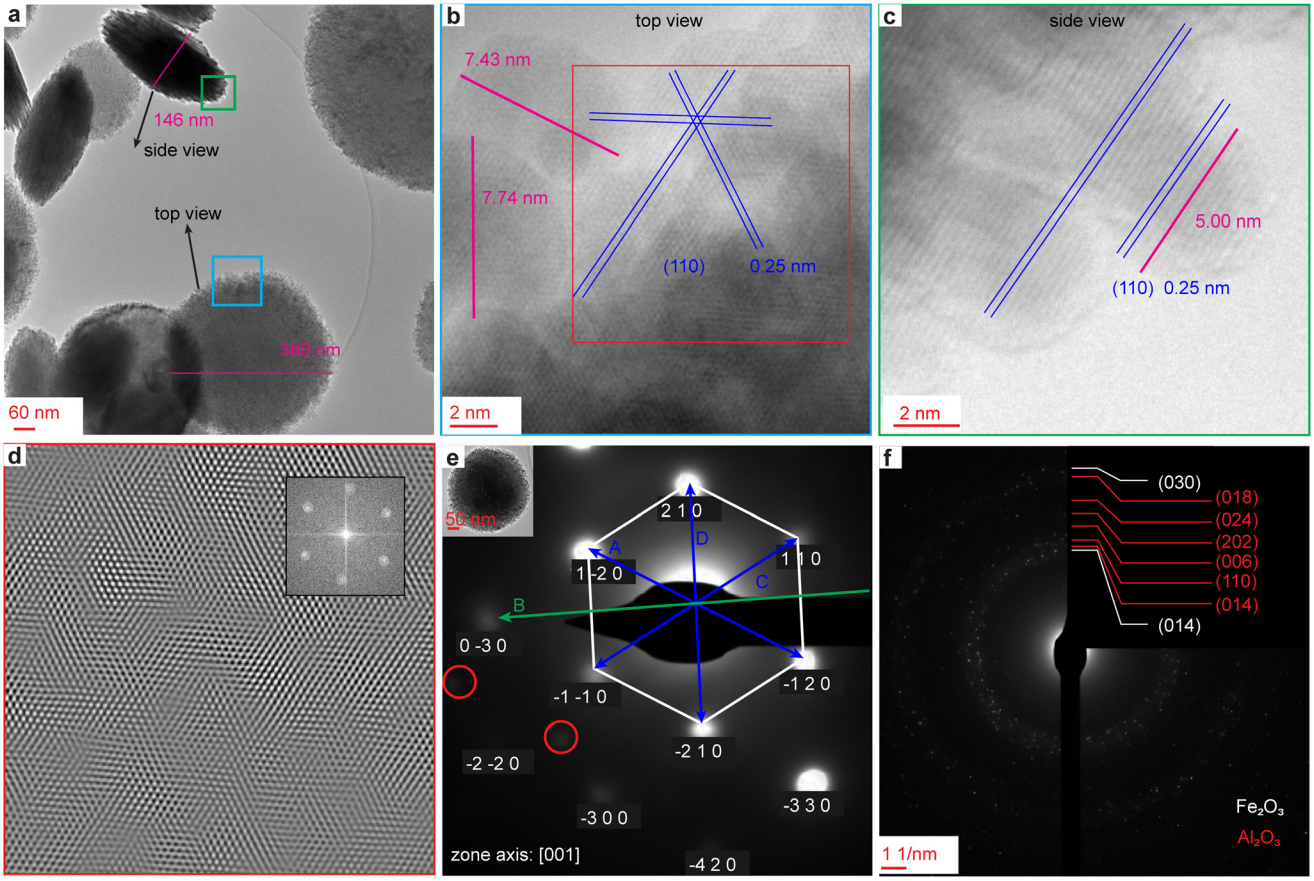

Fig. 3 High-resolution morphology and structures of the FeAl-4 (17.24 at%) sample. (a) TEM image showing the top and side view of the round nanoplates. (b) HRTEM image of the top surface of the highlighted cyan box region in (a). (c) HRTEM zoomed-in image of the highlighted green box region in (a), *i.e.*, the side-view of one nanoplate. (d) Inverse FFT image of the highlighted red box region in (b). The inset is the corresponding FFT image. (e) SAED pattern of one nanoplate (inset) showing a single crystal pattern. (f) SAED pattern of a group of nanoplates indicating the existence of two phases.

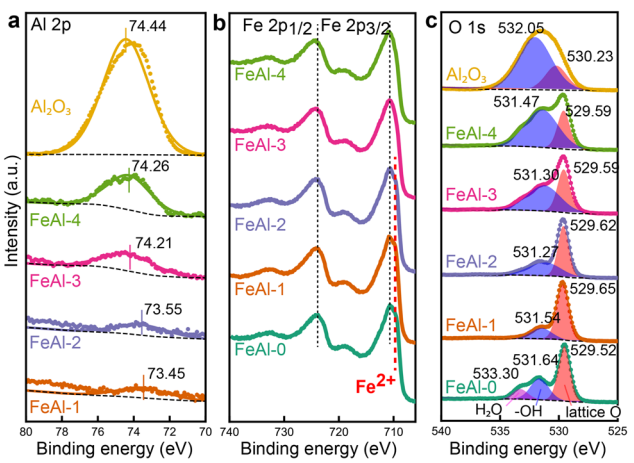

Fig. 4 XPS analysis of the surface properties. (a) Al 2p, where dotted data are from experiments, coloured lines are fitting curves, and black dotted lines are the background. (b) Measured XPS data for Fe 2p. (c) XPS data for O 1s, where dotted data are from experiments, coloured lines are fitting curves, and black dotted lines are the background.

surface enrichment and segregation of Al. This is further reflected in Fig. 4 for the subtle and obvious difference between the five samples. As evidenced by the Al 2p XPS profile, the peak positions for FeAl-1 and FeAl-2 with low Al concentration are located at 73.45 and 73.55 eV, respectively. These positions are slightly left-shifted in comparison with those of FeAl-3 and FeAl-4, which are instead much closer to that of the pure α-Al_2O_3 with a single peak of 74.44 eV. Clearly, a strong electron transfer occurs between the low-concentration Al and its surrounding Fe, whereas the other two high-Al samples are clearly clustered for its Al to show a similar local environment to the pure α-Al_2O_3. This agrees with the phase separation phenomenon revealed by the TEM analysis shown in Fig. 3f.

The Fe 2p XPS profile for pure hematite (*i.e.* FeAl-0) exhibits two peaks at 710.82 and 723.92 eV, corresponding to the characteristic signals of Fe^{3+} $2p_{2/3}$ and $2p_{1/2}$, respectively (Fig. 4b).[62] As the Al alloying content increases, these two peaks shift slightly to higher binding energies. Moreover, the Fe^{3+} $2p_{2/3}$ peak of FeAl-1 and FeAl-2 possesses a noticeable shoulder around 709 eV, which can be assigned to Fe^{2+}

$2p_{2/3}$.[1,62] The partial reduction of Fe^{3+} to Fe^{2+} could be due to the surface O vacancies created during the hydrothermal process, as in the case of the Ti^{3+} XPS shoulder found in TiO_2 samples.[63] Nevertheless, for the two low-Al samples of FeAl-1 and FeAl-2, the introduction of Al caused an insignificant change of the valence state of Fe^{3+} cations. However, for the two high-Al FeAl-3 and FeAl-4 samples, where phase separation and strong Al surface segregation were revealed, the Fe^{2+} $2p_{2/3}$ shoulder disappeared, suggesting that the surface O vacancies were preferentially occupied by Al. Likewise, the O 1s XPS of pure hematite (*i.e.* FeAl-0) can be deconvoluted to three symmetric peaks at 529.52, 531.64, and 533.30 eV, corresponding to the lattice O, surface hydroxyl, and adsorbed H_2O, respectively.[64] For the pure α-Al_2O_3, its O 1s XPS peak at 530.23 eV can be assigned to the lattice O, and the peak at 532.05 eV is for the surface hydroxyl. However, once Al is alloyed into hematite, the O 1s peak for the adsorbed H_2O vanishes, and the peak for surface hydroxyl content increases, closing to that of the pure α-Al_2O_3 for a strong adsorption of hydroxyl on the surface.

Phase diagram and phase separation of the (Fe, Al)$_2O_3$ alloy

Fig. 5a displays the mixing energy for the two metal oxides as a function of Al^{3+} concentration when the temperature was fixed as 0 K. Clearly, the DFT-computed mixing energies (blue circles) are almost identical with those predicted from the CE (yellow crosses), confirming the reliability of the trained CE model. Among the final 125 alloy structures used to train the active machine learning-like CE model, all the Al-alloyed hematite exhibits a positive mixing energy, indicating that the Al alloying to hematite and the Fe alloying to corundum are energetically unfavourable. Subsequently, the fully trained CE model was used as an energy functional in cooperation with MC simulations, which enabled us to plot the binary Al_2O_3–Fe_2O_3 phase diagram with the temperature ranging from 0 K to 1100 K. As shown in Fig. 5b, for the Al% range of 0 to 20 at% (the full concentration phase diagram is provided in Fig. S7†), and at the hydrothermal temperature of 453.15 K employed here, the last two samples of FeAl-3 and FeAl-4 fall into the shaded envelope where phase separation should occur. In contrast, the other two samples of FeAl-1 (1.01 at%) and FeAl-2 (2.88 at%) are in a single hematite phase with a high miscibility of Al^{3+} inside. This agrees with the experimental observation shown in Fig. 3.

MC simulations further revealed the spatial distribution of Al at varying temperatures. Taking FeAl-1 with 1 at% Al^{3+} as an example, Fig. 5c shows a homogeneous distribution of Al atoms in a disordered phase that is stable at the synthesis temperature of 450 K and also even down to 270 K, which is close to room temperature. With the temperature reduced further down to the phase transition temperature, 265 K, and below, the Al atoms aggregate into the discrete nanosized oxide (*i.e.*, α-Al_2O_3) and are precipitated out. In addition,

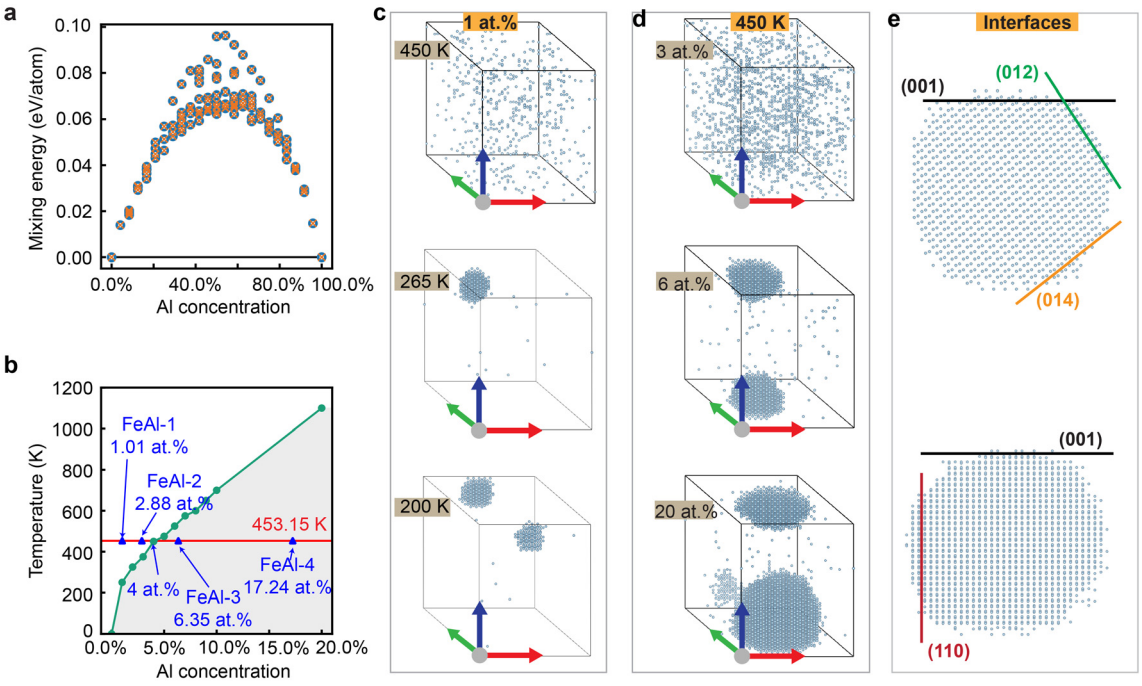

Fig. 5 Cluster expansion and Monte Carlo simulations for the (Fe, Al)$_2O_3$ alloy. (a) Mixing energy *vs.* Al concentration for 125 alloy configurations. The blue circles are DFT calculation results; yellow cross symbols represent the CE predictions. A black line connects the two ground states. (b) The calculated phase diagram of the (Fe, Al)$_2O_3$ system with Al concentrations ranging from 0 to 20.0%. The solid red line indicates the temperature to synthesise (Fe, Al)$_2O_3$ in our experiments. (c) Alloy microstructures at an Al concentration of 1 at% at various temperatures. (d) At 450 K (about the synthesis temperature), the microstructures of (Fe, Al)$_2O_3$ at different Al concentrations. (e) Interfaces between Al_2O_3 nano-precipitates and Fe_2O_3 bulk matrix at the Al concentration of 20 at% at 450 K. For clarity, figures (c), (d), and (e) only show Al atoms.

Fig. 5d reveals the spatial distribution of Al with varying concentrations at 450 K. Below 4 at%, the Al atoms homogenously distribute inside the (Fe, Al)$_2$O$_3$ bulk matrix. When the Al% exceeds 4 at%, quasi-spherical precipitates dominate for 6 at% and 20 at% (*i.e.*, FeAl-3 and FeAl-4). This quasi-spherical precipitate also demonstrates the predominance of (001), (110), (012), and (014) surfaces as the interfaces with the bulk hematite as shown in Fig. 5e. The formation of α-Al$_2$O$_3$ agrees well with the observed corundum phase detected using SAED as shown in Fig. 3f.

Specific surface energies for the surfaces of (Fe, Al)$_2$O$_3$

Although the MC simulations revealed the phase separation, it requires surface energy and Wulff construction to understand the morphological evolution and the (001) surface dominance. The pure α-Fe$_2$O$_3$ in a vacuum was first modelled as a reference. The conventional unit cell of pure α-Fe$_2$O$_3$ is made up of twelve Fe and eighteen O atoms belonging to the $R\bar{3}c$ space group (Fig. S8a†). The twelve Fe atoms can be divided into six groups along the lattice c direction, whilst the eighteen O atoms sandwich the adjacent groups. The pure hematite phase of α-Fe$_2$O$_3$ has an anti-ferromagnetic ground state, with opposite magnetic moments between two adjacent Fe atom groups. The lattice parameters of hematite were calculated using DFT as $a = b = 5.05$ Å and $c = 13.79$ Å, which are close to the experimentally reported values ($a = b = 5.04$ Å, and $c = 13.75$ Å).[65] The magnetic moment at each Fe atom was calculated to be $4.19\mu_B$, agreeing satisfactorily with the experimental Fe magnetic moment of $4.9\mu_B$.[66] The density-of-states (DOS) plot in Fig. S8b† also indicates that hematite is a semiconductor with a band gap of 2.06 eV, matching the experimentally observed value of 2.0 eV.[66,67]

Four slab models for the (001), (012), (101), and (110) surfaces of hematite were built, as shown in Fig. 6a and Fig. S9.† These four surfaces were selected as they have proven essential for a satisfactory prediction of the hematite morphology.[68,69] Note that although the (014) surface shows a strong signal in XRD patterns (Fig. 2a), it was omitted in our theoretical simulations, as the strong XRD signal does not guarantee surface exposure,[70] and Souza *et al.* already reported that the (014) surface has much higher specific surface energy than that of the selected four surfaces, which leads to its vanishing in the predicted morphology.[68] The surface area (A) values of the four slab supercells are 22.08, 82.46, 73.06, and 120.62 Å^2, respectively. The calculated γ values are summarised and compared with other reported values in Table 2 and Table S3.†[71–77] Our calculated surface energies are 1.33, 1.22, 1.41, and 1.44 J m^{-2} for the (001), (012), (110), and (101) surfaces, respectively, which are close to those from Guo *et al.*'s work.[74] Specific surface energy deviations from other works are mainly due to the different computing methods.[72,73,75] Regardless, it is conclusively shown that the hematite (012) surface is the most stable surface, showing the least specific surface energy (γ). Subsequently, the specific surface energy for the surface of the Al-alloyed hematite was computed.

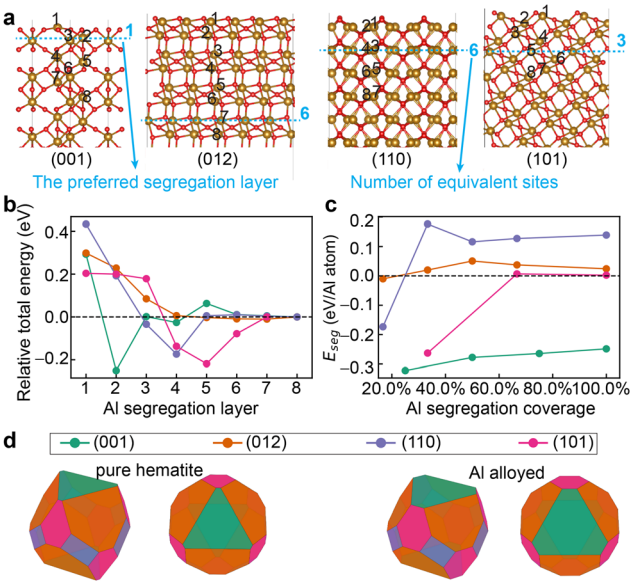

Fig. 6 DFT calculations for surface segregation energy and predicted particle morphology using the Wulff construction method. (a) The hematite (001), (012), (110), and (101) surface slab models. The dashed blue lines represent the preferred Al alloying layer. The numbers of equivalent sites are also shown. (b) The relative total energy of surface slab models with an Al atom at different locations. The most negative energy represents the surface segregation energy. (c) Surface segregation energy as a function of segregated Al. (d) The predicted equilibrium particle morphology of pure hematite and Al-alloyed hematite nanoparticles, using the Wulff construction method. The colour schemes of (b), (c), and (d) are the same.

Table 2 DFT-calculated specific surface energies γ (J m^{-2}) for pure Fe$_2$O$_3$

Surfaces	γ	Ref. 72	Ref. 73	Ref. 74	Ref. 75
(001)	1.33	1.53	0.76	1.14	2.30
(012)	1.22	1.47	0.54	1.06	1.96
(110)	1.41	—	0.81	1.23	—
(101)	1.44	2.41	1.16	1.31	2.84

A dopant usually has lower energy on the surface than inside the bulk matrix;[78,79] thus, it can cause surface segregation, as revealed by our XPS examinations. Here, the energy difference between surface and bulk is defined as the segregation energy (E_{seg}), as seen in eqn (2), which is highly dependent on the position of the doping layer and coverage of the Al dopant on a surface. Furthermore, to determine the layer-dependent value of the E_{seg}, we substituted one Al atom at different Fe layers of each pure hematite surface. These layers are labelled with black numbers in Fig. 6a. This figure also marks the preferred segregation layer, as shown by the blue dashed line with the most negative relative total energy, and the assigned blue number indicates the number of equivalent sites at each preferred segregation layer. Fig. 6b shows the DFT-calculated relative total energy results for a single Al atom at the i^{th} layer. The relative total energy gradually converges

and dissipates with the Al atom penetrating deep into the eighth layer. Hence, we used the eighth layer to represent the bulk layer, and the E_{seg} is then referred to as the relative energy between the preferred segregation layer and the eighth layer.

In addition, it is also evident that the second layer for the (001) hematite surface is the preferred segregation layer with an E_{seg} = −0.25 eV per Al atom. Likewise, for the (012), (110), and (101) surfaces, the preferred segregation location is the seventh, fourth, and fifth layer that exhibits an E_{seg} value of −0.01, −0.17, and −0.22 eV per Al atom, respectively. By defining the segregation coverage as the number of occupied sites divided by the number of all the equivalent sites, the segregation coverage of the calculated E_{seg} above reaches 100% for the (001) surface, 33.33% for the (101) surface, and 16.67% for the (012) and the (110) surface. Here, our simulations explain the XPS data given in Table 1 that the Al% on surfaces is higher than the Al% in bulk because Al intends to segregate on surfaces.

We also calculated the E_{seg} at other segregation coverages using the same solute atom segregation layer. Configurations for different coverages on the four hematite surfaces are illustrated in Fig. S10–S13 and Tables S4, 5.† Generally, as plotted in Fig. 6c, increasing the Al^{3+} segregation coverage causes the E_{seg} to increase. Furthermore, as positive E_{seg} values indicate unfavourable surface segregation, only the negative E_{seg} values matter. For the (001) surface, its E_{seg} always remains negative. In contrast, for the other three surfaces, the E_{seg} only remains negative for a low Al coverage, *e.g.*, 16.67% for the (012) and the (110) and 33.33% for the (101) surface. The (001) surface is the one where the surface segregation is the most remarkable, as the surface segregation coverage that can be achieved is 100%.

Using these negative E_{seg} values at the highest segregation coverages, we updated the specific surface energy of each surface after the alloying with Al^{3+}, as defined by γ', according to eqn (2). Correspondingly, the specific surface energy (γ') reaches 1.15 J m^{-2} for the (001) surface at 100% coverage, relative to 1.22 J m^{-2} and 1.39 J m^{-2} for the (012) and the (110) surfaces at 16.67% coverage, respectively, and 1.38 J m^{-2} for the (101) surface at 33.33% coverage. The alloying of Al^{3+} clearly makes the hematite (001) surface the most stable.

Furthermore, taking the specific surface energies computed above as input values, the Wulff construction method was used to construct the equilibrated morphology of Al-alloyed hematite.[80] As depicted in Fig. 6d, the pure Fe_2O_3 shows a C_3 rotation symmetry and a spherical outlook from the top view. Its exposed (001) surface is also in a triangle shape, and the area fraction of this surface reaches 13.64%. In contrast, as the (012) surface of pure Fe_2O_3 exhibits the lowest specific surface energy (Table 2), it presents the most prominent area fraction of 55.93%. The Al surface segregation reduces the specific surface energy of the (001) surface down to 1.15 J m^{-2}, and the predicted (001) surface has an area percentage of 19.43%, which is considerably higher than the (001) surface for the pure hematite. Nevertheless, the predicted overall shape is still nearly spherical, without exhibiting any flattening feature as opposed to the experimental observations shown in Fig. 2.

Ethanol capping agent effect

Third, the capping agent ethanol was explored in terms of its potential role in affecting the growth and morphology of hematite. Considering the steric effect, we found that the 2 × 2 × 1 supercell of the (001) surface for pure hematite can chemisorb maximally four ethanol molecules, and the (012), (101), and (110) surfaces can chemisorb maximally three, three, and six ethanol molecules, respectively (Fig. S14†).

Consequently, the coverage-dependent adsorption energy (E_{ads}) of ethanol and the corresponding specific surface energy (γ_{eth}) are plotted in Fig. 7a. For the (012), (110), and (101) surfaces, the E_{ads} is less negative as the coverage of ethanol increases. In contrast, the E_{ads} for the (001) surface becomes more negative with the increment of the coverage, suggesting a self-promoting chemisorption effect of ethanol on the (001) surface. Indeed, the chemisorption of ethanol stabilises the surface and decreases the specific surface energy significantly, as evidenced in Fig. 7b. Given the adsorption coverage above 50%, the (001) surface becomes the most stable surface for the pure hematite. In particular, in the case of full coverage of ethanol, the specific surface energy of the (001) surface is down to only 0.31 J m^{-2}, relative to 0.55 J m^{-2} for the (012) surface. Finally, as the specific surface energy presents a linear relation *versus* the coverage of ethanol (Fig. S15†), we further predicted the specific surface energy values and constructed the equilibrium particle shapes at different ethanol surface adsorption coverages.

As shown in Fig. 7c, the morphology slightly changes from 0% to 50% ethanol adsorption. A relatively more significant morphology change occurs beyond 75%. At 100% coverage, the

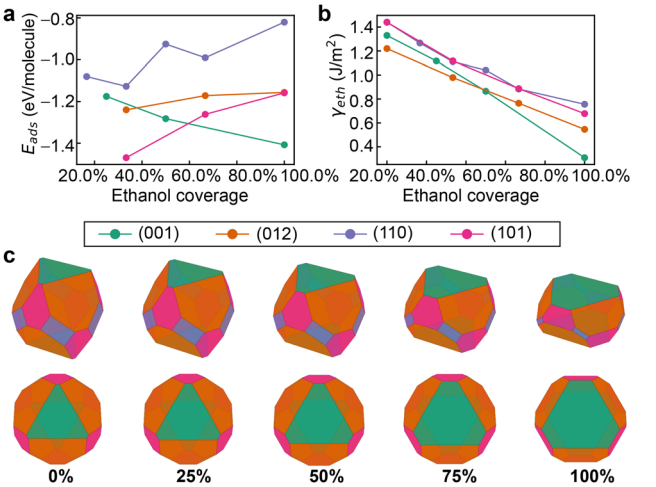

Fig. 7 Capping agent effect on the specific surface energy and the resultant morphology change predicted by the Wulff construction method. (a) Ethanol coverage-dependent adsorption energy. (b) Ethanol coverage-dependent specific surface energy. (c) The equilibrium Wulff morphology of hematite under various ethanol coverages. The colour schemes of (a), (b), and (c) are the same.

shape of the exposed (001) surface is closer to a hexagon, and its area fraction increases to 36.13%. The 100% ethanol coverage stabilises the hematite (001) surface to promote a flat nanoparticle with an aspect ratio of 2.05. However, the relatively small area fraction, 36.13%, of the (001) surface still shows a significant discrepancy from observation as revealed in Fig. 2f.

Synergistic effect between Al and ethanol

Finally, we considered the co-existence of cationic Al and ethanol on the hematite surface. Note that we did not consider H_2O as a capping agent even though it exists during the hydrothermal treatment because H_2O was revealed to facilitate the nucleation rather than confining the morphology.[25] Although these sample surfaces are covered with hydroxyl groups, as shown in Fig. 5c, the surface hydroxyl was not referred to as a capping agent since the hydroxyl group mainly originates from the dissociative adsorbed H_2O after the formation of surfaces.[20] As shown in Fig. 8a, for the (001) surface, the second layer of Fe sites remains the preferred alloying layer for Al, the same as in Fig. 8 for the absence of ethanol. However, the E_{seg} at the Al coverage of 100% changes to −0.17 eV per Al atom, relative to the value of −0.25 for the bare (001) surface. The preferred Al segregation layer on the (012), (110), and (101) surfaces changes to the third, sixth, and first layer, and the corresponding E_{seg} value is −0.02 (16.67%), −0.10 (16.67%), and −0.33 eV per Al atom (33.33%), respectively. Overall, the changes in E_{seg} are insignificant. Based on the results in Fig. 6c, it is reasonable to expect that the E_{seg} for Al on the (012), (110), and (101) surfaces would become positive when the Al coverage increases. Thus, only the E_{seg} for Al on the (001) surface was investigated further for its coverage-dependent trend. In Fig. 6c, the E_{seg} for Al on the bare (001) surface becomes monotonously less negative as the Al coverage increases. In contrast, after ethanol caps the (001) surface, the E_{seg} oscillates between −0.30 and −0.17 eV per Al atom (Fig. S16†).

Due to the segregation, the specific surface energy of the (001) surface further reduces as the Al coverage increases (Fig. 8b). Following this, based on the Wulff construction method, we constructed the equilibrated Al-alloyed Fe_2O_3 nanoparticle morphology with a full ethanol coverage and varying Al coverage on the (001) surface (Fig. 8c). Once Al is alloyed into the ethanol-adsorbed hematite surfaces, the (110) surface disappears due to its relatively high specific surface energy. The morphology of the nanoparticle is also gradually flattened, whereas the shape of the exposed (001) surface gets closer to a hexagon. The overall shape is consistent with our experimental observation for the two high-Al content samples as shown in Fig. 2 and 3. More importantly, at the 100% Al coverage, the area fraction of the (012) surface declines to 21.32%, while that of the (001) surface dominates (59.95%). Accordingly, it is conclusively demonstrated that the morphological evolution of hematite nanoparticles is attributed to the synergy between cationic Al dopant and the capping agent ethanol during the hydrothermal synthesis procedure.

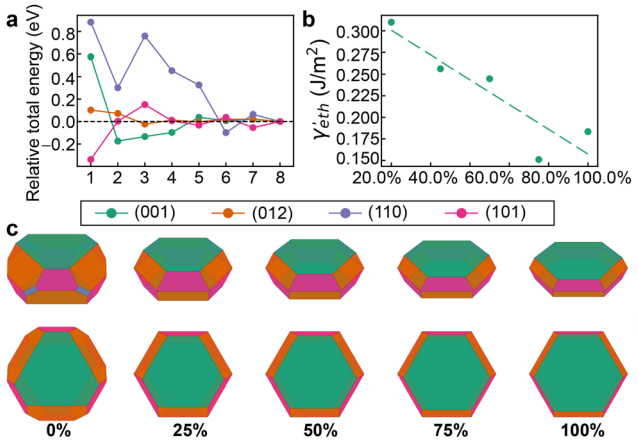

Fig. 8 The synergistic effect of Al segregation and ethanol surface adsorption on the morphology of the Al-alloyed hematite. (a) The relative energy of segregated Al atoms at different sub-surface locations. (b) (001) Surface energy as a function of Al segregation concentration with full ethanol surface adsorption. (c) The predicted Al-alloyed hematite nanoparticle morphology under the capping of ethanol and at various Al coverages. The colour schemes of (a), (b), and (c) are the same.

Conclusions

In this work, we successfully synthesised (001) surface-dominated aluminium-alloyed hematite round nanoplates using co-precipitation and hydrothermal methods with a fixed ethanol/water volume ratio of 30 : 70 at 180 °C. We observed the nanoparticle morphological evolution from rhombohedron to round nanoplate when the Al alloying concentration of aluminium is ≥6.35 at%. These round nanoplates are assembled by smaller individual particles in a crystallographic orientation, exhibiting a monocrystalline electron diffraction pattern and exposing the dominant (001) surface. We explained this phenomenon based on phase separation and surface energy computed from the combined use of DFT, CE, and Monte Carlo simulations. The phase diagram constructed from the modelling suggests a threshold concentration of 4 at% for Al. Any concentration above this causes phase separation with the formation of discrete α-Al_2O_3 nanoparticles. Information from the Monte Carlo simulations and phase diagram was used to build surface models for the Fe-rich phase. DFT calculations revealed that aluminium segregates intensively on the hematite (001) surface. Such surface segregation of aluminium can stabilise the hematite (001) surface whilst it exerts marginal change to the entire morphology of the hematite nanoparticle. In contrast, the capping agent ethanol and its adsorption alone in the absence of Al^{3+} can reduce the specific surface energy of the hematite (001) surface from 1.33 to 0.31 J m^{-2}, whilst the combined segregation of aluminium and adsorption of ethanol can synergistically drop the specific surface energy down to 0.18 J m^{-2}. Consequently, the (001) surface dominates the Al-alloyed hematite nano-

particles, and the hematite nanoparticles are flattened significantly.

Conflicts of interest

There are no conflicts to declare.

Acknowledgements

This work was funded by the Australian Research Council (LP180100128, LP190100849, LE21010010, DP200100204 and DP200100313). We thank the Monash Centre of Electron Microscopy (MCEM) for support with electron microscopy. This research was undertaken with the assistance of resources and services from the National Computational Infrastructure (NCI), which is supported by the Australian Government.

References

1 F. Kraushofer, Z. Jakub, M. Bichler, J. Hulva, P. Drmota, M. Weinold, M. Schmid, M. Setvin, U. Diebold, P. Blaha and G. S. Parkinson, *J. Phys. Chem. C*, 2018, **122**, 1657–1669.
2 Y. Yin, X. Zhang and C. Sun, *Prog. Nat. Sci.: Mater. Int.*, 2018, **28**, 430–436.
3 Z. Zhang, T. Tsuchimochi, T. Ina, Y. Kumabe, S. Muto, K. Ohara, H. Yamada, S. L. Ten-no and T. Tachikawa, *Nat. Commun.*, 2022, **13**, 1499.
4 G. Righi, J. Plescher, F.-P. Schmidt, R. K. Campen, S. Fabris, A. Knop-Gericke, R. Schlögl, T. E. Jones, D. Teschner and S. Piccinin, *Nat. Catal.*, 2022, **5**, 888–899.
5 K. Sivula, F. Le Formal and M. Grätzel, *ChemSusChem*, 2011, **4**, 432–449.
6 J. Deng, C. Ye, A. Cai, L. Huai, S. Zhou, F. Dong, X. Li and X. Ma, *Chem. Eng. J.*, 2021, **420**, 129863.
7 X. Liu, J. Liu, Z. Chang, X. Sun and Y. Li, *Catal. Commun.*, 2011, **12**, 530–534.
8 M. Zhu, T. C. R. Rocha, T. Lunkenbein, A. Knop-Gericke, R. Schlögl and I. E. Wachs, *ACS Catal.*, 2016, **6**, 4455–4464.
9 O. Yalcin, S. Sourav and I. E. Wachs, *ACS Catal.*, 2023, 12681–12691.
10 I. B. Bychko, G. R. Kosmambetova, Y. Y. Kalishyn, V. O. Khavrus, V. I. Gritsenko and P. E. Strizhak, *React. Chem. Eng.*, 2023, **8**, 2841–2848.
11 T. Takashima, S. Hemmi, Q. Liu and H. Irie, *Catal. Sci. Technol.*, 2020, **10**, 3748–3754.
12 B. Mohanty, Y. Wei, M. Ghorbani-Asl, A. V. Krasheninnikov, P. Rajput and B. K. Jena, *J. Mater. Chem. A*, 2020, **8**, 6709–6716.
13 S. Rehman, W. Yang, F. Liu, Y. Hong, T. Wang and Y. Hou, *Inorg. Chem. Front.*, 2015, **2**, 576–583.
14 T. Guo, L. Jiang, K. Wang, Y. Li, H. Huang, X. Wu and G. Zhang, *Appl. Catal., B*, 2021, **286**, 119883.
15 M. Zong, D. Song, X. Zhang, X. Huang, X. Lu and K. M. Rosso, *Environ. Sci. Technol.*, 2021, **55**, 677–688.
16 J. Lu, Q. Peng, Z. Wang, C. Nan, L. Li and Y. Li, *J. Mater. Chem. A*, 2013, **1**, 5232.
17 Z. Lyu, S. Niu, C. Lu, G. Zhao, Z. Gong and Y. Zhu, *Fuel*, 2020, **267**, 117147.
18 N. Kumar, N. Seriani and R. Gebauer, *Phys. Chem. Chem. Phys.*, 2020, **22**, 10819–10827.
19 M.-F. Ng, D. J. Blackwood, H. Jin and T. L. Tan, *J. Phys. Chem. C*, 2020, **124**, 13799–13808.
20 J. L. Junta-Rosso and M. F. Hochella, *Geochim. Cosmochim. Acta*, 1996, **60**, 305–314.
21 Y. Liang, M. Wang, J. Xiong, J. Hou, X. Wang and W. Tan, *Environ. Sci. Nano*, 2019, **6**, 1323–1331.
22 B. Qian, C. Liu, J. Lu, M. Jian, X. Hu, S. Zhou, T. Hosseini, B. Etschmann, X. Zhang, H. Wang and L. Zhang, *J. Hazard. Mater.*, 2020, **395**, 122696.
23 W. Li, X. Liang, P. An, X. Feng, W. Tan, G. Qiu, H. Yin and F. Liu, *Sci. Rep.*, 2016, **6**, 35960.
24 W. Wang, W. Zhang, Y. Fan, C. Qu, W. Ren, X. Huang, M. Hong, F. Liu and H. Yin, *Environ. Sci. Nano*, 2022, **9**, 2073–2085.
25 L. Chen, X. Yang, J. Chen, J. Liu, H. Wu, H. Zhan, C. Liang and M. Wu, *Inorg. Chem.*, 2010, **49**, 8411–8420.
26 J. Cai, S. Chen, M. Ji, J. Hu, Y. Ma and L. Qi, *CrystEngComm*, 2014, **16**, 1553–1559.
27 M. Zong, X. Zhang, Y. Wang, X. Huang, J. Zhou, Z. Wang, J. J. De Yoreo, X. Lu and K. M. Rosso, *Inorg. Chem.*, 2019, **58**, 16727–16735.
28 R. Li, X. Zhang, H. Dong, Q. Li, Z. Shuai and W. Hu, *Adv. Mater.*, 2016, **28**, 1697–1702.
29 D. J. Cooke, S. E. Redfern and S. C. Parker, *Phys. Chem. Miner.*, 2004, **31**, 507–517.
30 M. Alfredsson, F. Corà, D. P. Dobson, J. Davy, J. P. Brodholt, S. C. Parker and G. D. Price, *Surf. Sci.*, 2007, **601**, 4793–4800.
31 S.-H. Liu, T. Balankura and K. A. Fichthorn, *Phys. Chem. Chem. Phys.*, 2016, **18**, 32753–32761.
32 A. C. Turnock and H. P. Eugster, *J. Petrol.*, 1962, **3**, 533–565.
33 A. D. Polli, F. F. Lange, C. G. Levi and J. Mayer, *J. Am. Ceram. Soc.*, 1996, **79**, 1745–1755.
34 C. E. Meyers, T. O. Mason, W. T. Petuskey, J. W. Halloran and H. K. Bowen, *J. Am. Ceram. Soc.*, 1980, **63**, 659–663.
35 M. Klinger and A. Jäger, *J. Appl. Crystallogr.*, 2015, **48**, 2012–2018.
36 M. Klinger, *J. Appl. Crystallogr.*, 2017, **50**, 1226–1234.
37 D. Kleiven, J. Akola, A. A. Peterson, T. Vegge and J. H. Chang, *J. Phys. Energy*, 2021, **3**, 034012.
38 J. H. Chang, D. Kleiven, M. Melander, J. Akola, J. M. Garcia-Lastra and T. Vegge, *J. Phys.: Condens. Matter*, 2019, **31**, 325901.
39 Q. Li, M. Rellán-Piñeiro, N. Almora-Barrios, M. Garcia-Ratés, I. N. Remediakis and N. López, *Nanoscale*, 2017, **9**, 13089–13094.
40 Md. M. Hasan, P. P. Dholabhai, R. H. R. Castro and B. P. Uberuaga, *Surf. Sci.*, 2016, **649**, 138–145.

41 A. V. Ignatchenko, *J. Phys. Chem. C*, 2011, **115**, 16012–16018.
42 G. D. Barmparis and I. N. Remediakis, *Phys. Rev. B: Condens. Matter Mater. Phys.*, 2012, **86**, 085457.
43 B. Zhu, Z. Xu, C. Wang and Y. Gao, *Nano Lett.*, 2016, **16**, 2628–2632.
44 G. Kresse and J. Furthmüller, *Comput. Mater. Sci.*, 1996, **6**, 15–50.
45 J. P. Perdew, K. Burke and M. Ernzerhof, *Phys. Rev. Lett.*, 1996, **77**, 3865–3868.
46 N. J. Mosey, P. Liao and E. A. Carter, *J. Chem. Phys.*, 2008, **129**, 014103.
47 P. Liao, M. C. Toroker and E. A. Carter, *Nano Lett.*, 2011, **11**, 1775–1781.
48 S. Piccinin, *Phys. Chem. Chem. Phys.*, 2019, **21**, 2957–2967.
49 S. Bandaru, G. Saranya, W. W. Liu and N. J. English, *Catal. Sci. Technol.*, 2020, **10**, 1376–1384.
50 V. Sinha, D. Sun, E. J. Meijer, T. J. H. Vlugt and A. Bieberle-Hütter, *Faraday Discuss.*, 2021, **229**, 89–107.
51 V. Wang, N. Xu, J.-C. Liu, G. Tang and W.-T. Geng, *Comput. Phys. Commun.*, 2021, **267**, 108033.
52 K. Momma and F. Izumi, *J. Appl. Crystallogr.*, 2011, **44**, 1272–1276.
53 M. Congiu, M. L. De Marco, M. Bonomo, O. Nunes-Neto, D. Dini and C. F. O. Graeff, *J. Nanopart. Res.*, 2016, **19**, 7.
54 A. K. Patra, S. K. Kundu, A. Bhaumik and D. Kim, *Nanoscale*, 2016, **8**, 365–377.
55 T. Ossowski, T. Pabisiak, A. Kiejna, K. Palotás and E. Bauer, *J. Phys. Chem. C*, 2021, **125**, 26711–26717.
56 R. Li, Q. Li, S. Gao and J. K. Shang, *J. Am. Ceram. Soc.*, 2011, **94**, 584–591.
57 S. Jiang, X. Yan, C. L. Peacock, S. Zhang, W. Li, J. Zhang, X. Feng, F. Liu and H. Yin, *J. Hazard. Mater.*, 2020, **390**, 122014.
58 J. S. Han, T. Bredow, D. E. Davey, A. B. Yu and D. E. Mulcahy, *Sens. Actuators, B*, 2001, **75**, 18–23.
59 Q. Xiao, Y. Sun, J. Zhang and Q. Li, *Appl. Surf. Sci.*, 2015, **356**, 18–23.
60 Y. NuLi, R. Zeng, P. Zhang, Z. Guo and H. Liu, *J. Power Sources*, 2008, **184**, 456–461.
61 A. Rufus, N. Sreeju, V. Vilas and D. Philip, *J. Mol. Liq.*, 2017, **242**, 537–549.
62 T. Yamashita and P. Hayes, *Appl. Surf. Sci.*, 2008, **254**, 2441–2449.
63 Y.-C. Ho, M. N. F. Hoque, E. Stoneham, J. Warzywoda, T. Dallas and Z. Fan, *J. Phys. Chem. C*, 2017, **121**, 23939–23946.
64 Q. Qin, T. Liu, J. Zhang, R. Wei, S. You and Y. Xu, *J. Hazard. Mater.*, 2021, **419**, 126447.
65 G. S. Parkinson, *Surf. Sci. Rep.*, 2016, **71**, 272–365.
66 Y. Meng, X.-W. Liu, C.-F. Huo, W.-P. Guo, D.-B. Cao, Q. Peng, A. Dearden, X. Gonze, Y. Yang, J. Wang, H. Jiao, Y. Li and X.-D. Wen, *J. Chem. Theory Comput.*, 2016, **12**, 5132–5144.
67 C. Haavik, S. Stølen, H. Fjellvåg, M. Hanfland and D. Häusermann, *Am. Mineral.*, 2000, **85**, 514–523.
68 J. C. Souza, R. A. P. Ribeiro, L. G. Da Trindade, R. C. D. Oliveira, L. D. Costa, M. C. De Oliveira, S. R. De Lazaro, J. R. Sambrano, C. R. Mendonça, L. De Boni, F. M. L. Pontes, A. J. A. De Oliveira, E. R. Leite and E. Longo, *ACS Omega*, 2021, **6**, 28049–28062.
69 A. C. Catto, M. C. Oliveira, R. A. P. Ribeiro, W. Avansi, L. F. Da Silva and E. Longo, *Appl. Surf. Sci.*, 2021, **563**, 150209.
70 J. Qu, Y. Wang, X. Mu, J. Hu, B. Zeng, Y. Lu, M. Sui, R. Li and C. Li, *Adv. Mater.*, 2022, **34**, 2203320.
71 W. C. Mackrodt, R. J. Davey, S. N. Black and R. Docherty, *J. Cryst. Growth*, 1987, **80**, 441–446.
72 W. C. Mackrodt, *Phys. Chem. Miner.*, 1988, **15**, 228–237.
73 A. L. Rohl and D. H. Gay, *J. Cryst. Growth*, 1996, **166**, 84–90.
74 H. Guo and A. S. Barnard, *J. Mater. Chem.*, 2011, **21**, 11566–11577.
75 N. J. Reeves and S. Mann, *J. Chem. Soc., Faraday Trans.*, 1991, **87**, 3875–3880.
76 N. Y. Dzade, A. Roldan and N. H. De Leeuw, *Minerals*, 2014, **4**, 89–115.
77 N. H. de Leeuw and T. G. Cooper, *Geochim. Cosmochim. Acta*, 2007, **71**, 1655–1673.
78 M. Polak and L. Rubinovich, *Surf. Sci. Rep.*, 2000, **38**, 127–194.
79 H. Liao, A. Fisher and Z. J. Xu, *Small*, 2015, **11**, 3221–3246.
80 E. Ringe, R. P. Van Duyne and L. D. Marks, *Nano Lett.*, 2011, **11**, 3399–3403.